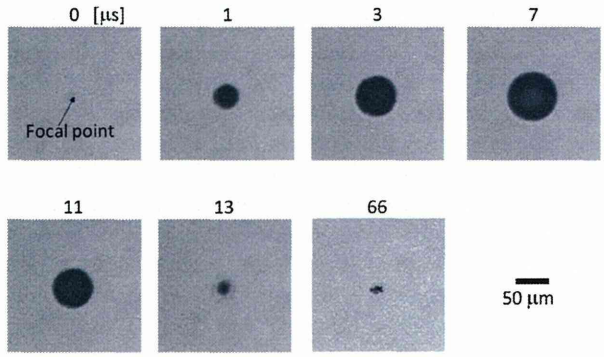

Fig. 4 Bright field images of HEWL supersaturated solutions monitored with a framing camera operating at 1×10^6 frames per s. The solutions were irradiated with a single femtosecond laser pulse. The arrow in the image at 0 μs indicates the laser focal point. Reprinted with permission from Springer, ref. 28, 2008.

To address this, Yoshikawa *et al.* carried out the high-speed imaging of supersaturated solutions of protein (HEWL), as shown in Fig. 4.[28] The round, black object observed at 1 μs is attributed to a cavitation bubble, which is formed by local boiling and/or vaporization of the supersaturated solutions. The single cavitation bubble expands and shrinks symmetrically in a few tens of microseconds. Finally, the cavitation bubble collapses, leaving some small "long-lasting" bubbles (at 66 μs in Fig. 4), which are considered to contain dissolved gases from the supersaturated solution.

On the basis of studies of laser ablation of water and biological materials,[7,29] the mechanism of such cavitation bubble formation can be explained as follows. When a near-infrared femtosecond laser pulse is tightly focused into a transparent liquid such as a protein solution, the intensity in the focal volume can become high enough to cause multi-photon absorption. Then, dense excited and ionized states of the solutes and solvent molecules are formed. The following rapid energy conversion results in an accumulation of heat and thermoelastic pressure within the absorbing volume, which increases the vapor pressure of the solution. Finally, cavitation bubbles are generated when the vapor pressure of the solution exceeds that of the atmosphere. In principle, such cavitation bubble formation can be induced in any liquid by pulsed laser irradiation having an energy above a certain threshold. The threshold energy for 200 fs pulses to induce cavitation bubbles in supersaturated solutions of HEWL was estimated to be 0.3 μJ per pulse with a 10× objective (NA 0.25) from the maximum diameters of the cavitation bubbles *vs.* pulse energy.[28]

For small organic compounds, it was revealed that nucleation occurs only when cavitation bubbles are induced by femtosecond laser ablation.[20–22] In particular, in the case of anthracene, circularly bent crystalline films were formed on a bubble surface (Fig. 5).[22] These results strongly suggest that cavitation bubbles are the key for triggering nucleation. To clarify whether cavitation bubbles are also involved in the mechanism for proteins, the influence of laser energy on the nucleation of HEWL was systematically investigated.[28] The statistical analysis revealed

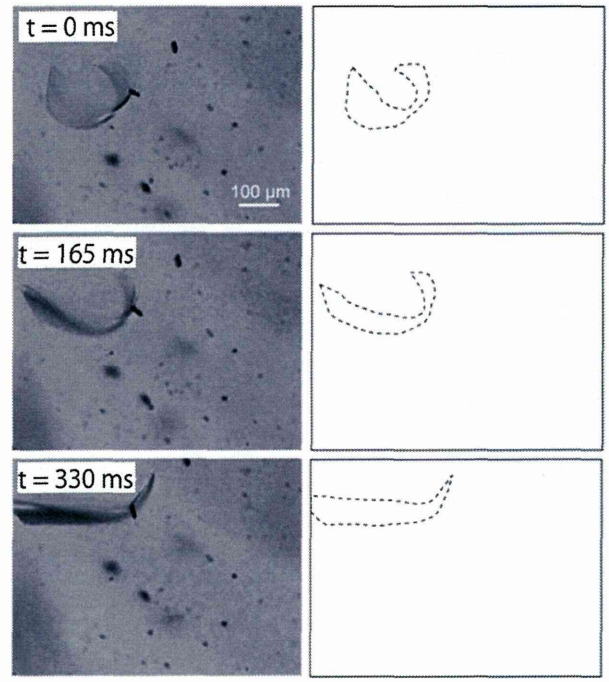

Fig. 5 Bright field images of bent film-like anthracene crystals generated with a single femtosecond laser pulse. The right side illustrations represent outlines of the crystal shown in the left side images. Reprinted with permission from American Chemical Society, ref. 22, 2007.

that the crystallization probability significantly increased beyond a laser energy of 0.4 μJ per pulse, while the crystallization probability below 0.4 μJ per pulse was the same as for the control (without laser irradiation). This threshold for nucleation, 0.4 μJ per pulse, is in good agreement with that for cavitation bubble formation (~0.3 μJ per pulse).

These results imply that cavitation bubbles induced by femtosecond laser ablation act as a trigger for nucleation of proteins as well as small organic compounds. To further clarify a protein nucleation mechanism based on laser-induced cavitation bubbles, fast imaging of protein concentration around cavitation bubbles was carried out using a fluorescent dye-labeled protein (F-lysozyme),[14,30] where the ε-amino group of the N-terminal lysine (Lys1) within each lysozyme molecule was chemically labeled with tetramethylrhodamine-5-isothiocyanate (5-TRITC, M_W 443 g mol^{-1}). Since the molecular weight of 5-TRITC is much less than that of native lysozyme (M_W 14 307 g mol^{-1}), the diffusion of F-lysozyme can be considered to be the same as that of native lysozyme. Fig. 6a shows fluorescence images of a supersaturated HEWL solution containing F-lysozyme and 2% agarose. The bright spot at 0 μs was attributed to plasma emission and scattering by an initial laser ablation process. The cavitation bubble expanded and shrank, and finally collapsed by 30 μs. Interestingly, at 20 μs, a bright spot with a peak intensity approximately three times larger than the average intensity of the surrounding gel medium was detected (Fig. 6b). This result indicates that cavitation bubbles induce the formation of a protein rich-region, which may lead to nucleation. In an alternative

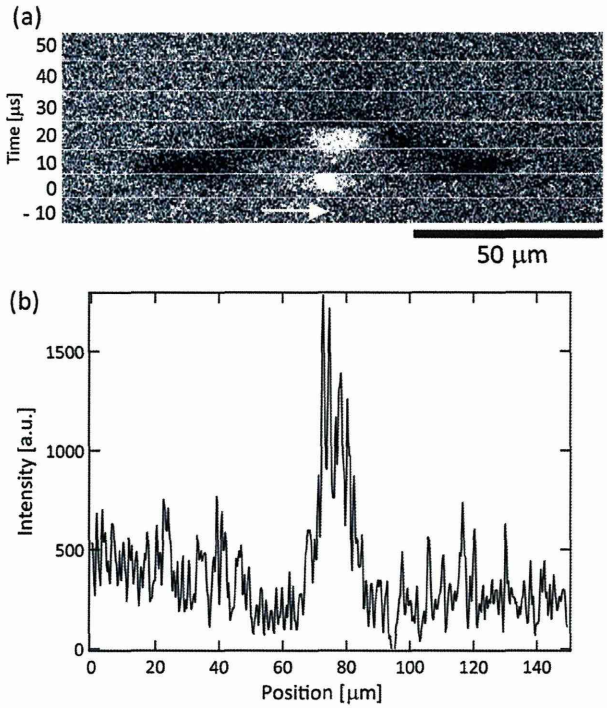

Fig. 6 (a) Fluorescence images of F-lysozyme in agarose gel. The samples were irradiated with a femtosecond laser pulse at 0 μs. The white arrow in the −10 μs image indicates the focal point of the laser. (b) Fluorescence intensity profile of (a) at 20 μs. Reprinted with permission from Springer, ref. 14, 2009.

approach to visualizing protein concentration around cavitation bubbles, Iefuji *et al.* used cytochrome *c*, which in solution is red in color due to the presence of heme groups.[31] They reported a clearer dynamics of formation of a highly concentrated protein region; a bright area (low concentration) was detected at the focal point (center of cavitation), and a dark area appeared around the cavitation bubbles (Fig. 7). Such dark and bright areas were not observed in pure water (absent proteins).

These results indicate that cavitation bubbles possibly induce the local condensation of protein molecules. Actually, an air-water interface is known to be preferable for protein nucleation and crystal growth.[32,33] In addition, evaporation of solvents may condense protein (and precipitants) near the bubble surface and result in nucleation. In fact, generation of the cavitation bubble is mainly due to the vaporization of water, not the other materials in the protein solution such as protein and precipitant, because there was no detectable difference in cavitation bubble size between the protein solution and pure water.[28] Furthermore, the shock wave[34] and the expansion and collapse of cavitation bubbles[35] generate a transient pressure with a magnitude reaching MPa–GPa. Such pressure fluctuations could also act as a nucleation trigger.[36]

In addition to the role of cavitation bubbles in nucleation, the photochemical effects of femtosecond laser-induced nucleation of proteins should be evaluated. Okutsu *et al.* reported that UV light produces photochemical covalently bonded protein dimers, which enhance nucleation.[37,38] The photochemical covalently bonded dimer of HEWL is considered to enhance nucleation because dimer formation *via* weak physical interactions (van der Waals force or hydrogen bonding) is energetically unfavorable. However, Murai *et al.* reported that the dimer contribution to nucleation is rather small in the femtosecond laser case, because the enhancement of nucleation by laser irradiation at λ = 260 nm (producing more dimers) is the same as that at λ = 780 nm.[39] One of the reasons why the contribution is small in the femtosecond laser case may be because femtosecond laser ablation would cause rather protein denaturation than dimer formation in the absorption volume. Murai *et al.* found that focused femtosecond laser irradiation produced not only dimers but also white, visibly large aggregates of denatured HEWL, which did not act as seeds for nucleation.[39] Since a femtosecond laser has a higher peak intensity [~GW] than a Xe lamp [~100 W], proteins rather undergo the simultaneous and/or stepwise multiphoton absorption, which can produce the permanently damaged species.[37]

Fig. 8 shows the currently considered mechanism of femtosecond laser-induced nucleation of proteins. Cavitation bubbles formed by femtosecond laser ablation increase the protein (and precipitant) concentration (supersaturation) locally and transiently in supersaturated solutions. Such a condensed region is relaxed due to the spontaneous diffusion of protein molecules. Hence, crystal nuclei which are generated by the transient increase in supersaturation grow slowly at lower supersaturation, and thus

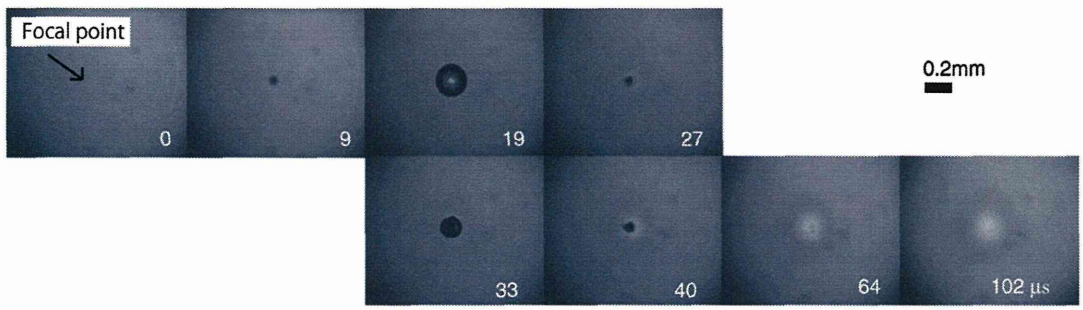

Fig. 7 Bright field images of cavitation bubbles induced by focusing a single femtosecond laser pulse into a cytochrome *c* solution. Reprinted with permission from Springer, ref. 31, 2011.

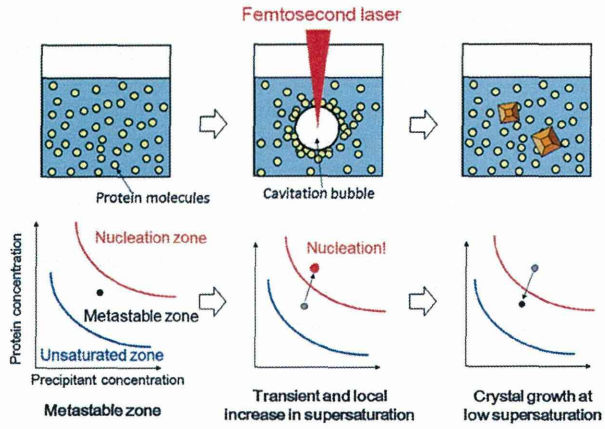

Fig. 8 Mechanism of femtosecond laser-induced protein nucleation.

high-quality crystals can be obtained. This is an ideal approach to overcome the persistent dilemma in protein crystallization. Cavitation bubbles can be generated by ultrasonication instruments, which have been utilized in protein crystallization.[40] However, transducers should be in contact with solutions to focus ultrasonic waves in small droplets (nL–μL, which is the standard volume for protein crystallization). On the other hand, a femtosecond laser can stimulate a tiny region (~μm) of such small droplets in a non-contact manner. Thus, the femtosecond laser technique would be easier for protein crystallization in practice. In addition, femtosecond laser ablation *via* multiphoton absorption[6] and photomechanical processes[7] can induce cavitation bubbles with less heat compared with longer laser pulses (*e.g.*, nanosecond lasers). When a near-infrared femtosecond laser pulse is tightly focused into a protein solution, the intensity in the focal volume can become high enough to cause multiphoton absorption, which then restricts the energy deposition within the absorbing volume and minimizes the collateral thermal damage. Also, the following rapid energy conversion results in an accumulation of heat and thermoelastic pressure within the absorbing volume, which increases the vapor pressure of the solutions. Finally, cavitation bubbles are generated when the vapor pressure of the solution exceeds that of the atmosphere. Thus, in the absence of photochemical decomposition (usually the case for proteins), a cavitation bubble generation process by femtosecond laser ablation of protein solutions is involved in the elevation of not only temperature but also thermoelastic pressure. In fact, there are a significant number of experimental observations suggesting that femtosecond laser ablation can be initiated at energy densities much lower than those required for boiling and vaporization.[7,41] Such energetically efficient cavitation bubble generation by femtosecond laser ablation, of course, is advantageous to the crystallization of proteins whose structures are sensitive to the surrounding temperature.

For protein nucleation, past studies strongly suggest that a cavitation bubble induced by laser ablation is a primary trigger. Nevertheless, other potential triggers such as the photochemically formed dimers[37,38] and the optical Kerr effect[2] should not be ruled out completely, because femtosecond laser pulses anyway provide high photon density and are also absorbed at a focal point. These may have to be taken into account on a case-by-case basis depending on protein properties. However, in other words, this implies that the femtosecond laser technique is a mixed approach which employs elements of other light-induced nucleation techniques as well as cavitation bubbles induced by laser ablation. This may be one of the reasons why the femtosecond laser is effective in inducing nucleation in a variety of materials. In addition, Knott *et al.* recently reported that unfocused laser pulses such as nanosecond lasers can induce bubble nucleation, and that small bubbles can induce crystal nucleation.[42] This suggests that extremely small (possibly nanoscale) and transient bubbles may form in the nucleation experiment by the optical Kerr effect[5] and catalyze crystal nucleation without being observed.[42] Thus, further studies on the mechanism of light-induced nucleation should consider multiple factors.

3. Laser ablation for protein crystal seeding

Crystal growth after nucleation is also a challenging step in obtaining high-quality, protein single crystals for X-ray crystallographic structural studies. Even if the environmental chemical and physical parameters (*e.g.*, temperature, solvent, and cosolutes) are carefully adjusted, irregularly shaped crystals (*e.g.*, polycrystals and cracked crystals) which are not suitable for crystallography are often obtained. One way that irregularly shaped crystals can be used is to produce single crystalline seeds by cutting or crushing the crystals with mechanical tools such as Micro-Tools (Hampton Research, USA). The seeds can be used for macroseeding or microseeding, which usually grows single crystalline seeds with the size of typically 5–50 μm (macroseeding) or much smaller (microseeding) in less supersaturated solutions.[2] However, special handling is required to cut or crush protein crystals with mechanical tools because protein crystals are soft, fragile, sensitive to changes in their surroundings, and in some cases very small (≤100 μm per dimension). To overcome the difficulties in processing protein crystals for macroseeding and microseeding, laser ablation is promising to produce crystal seeds by non-contact means. In this section laser ablation techniques are reviewed involving a pulsed deep-UV laser for macroseeding and a femtosecond laser for microseeding.

3.1. Macroseeding by deep-UV laser ablation

A pulsed deep-UV laser is one of the light sources which can be used for spatially precise, soft processing of protein crystals by laser ablation. Proteins have a broad absorption spectrum below the wavelength of 300 nm. In particular, the absorption coefficient below 200 nm is known to be twenty times larger than that at the 280 nm absorption peak.[43] Deep UV light ($\lambda <$ 200 nm) can cause direct photochemical decomposition of C–C and C–N bonds in the peptide linkage. Thus, the use of deep UV pulses enables laser ablation based on a photochemical decomposition process, which is desirable in order to reduce thermal

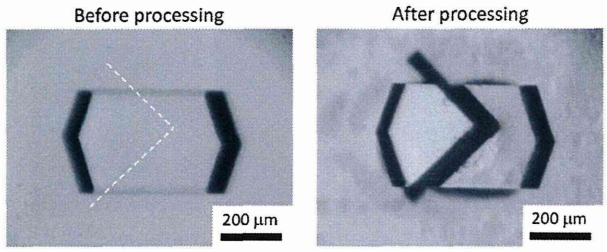

Fig. 9 Bright field images of a HEWL crystal before and after deep-UV laser ablation. The laser was scanned along the white dotted lines. Reprinted with permission from SPIE, ref. 10, 2007.

damage to the crystal. In addition, such photochemical laser ablation restricts the ablated region within the absorbing volume due to high absorbance and low heat generation. Kitano *et al.* demonstrated that deep-UV (λ = 193 nm) laser ablation enables processing of protein crystals of arbitrary shapes.[12] Fig. 9 shows representative examples of a HEWL crystal before and after laser ablation. The original crystal was divided into two parts by scanning the deep-UV laser pulses in *xyz* directions. No visible signs of cracks or denaturation were observed. The cross section was very sharp, and the nonirradiated parts of the crystal retained their original shape. It has also proven possible to obtain other shapes including a rectangle and a doughnut-like crystal.[20] Such shaping of protein crystals is, of course, extremely difficult to accomplish using conventional mechanical tools. To confirm the quality of the laser-irradiated crystal, the XRD pattern of the cut HEWL crystal was measured. The crystal diffracted beyond 1.9 Å resolution, which was the same as that of the as-grown HEWL crystal obtained under identical growth conditions. Fine processing using the deep-UV laser has been applied to various proteins, including GI, human lysozyme, phosphoenolpyruvate carboxylase, and AcrB without deterioration of the XRD data.[44,45]

Crystals processed by deep-UV laser ablation can be used for macroseeding. A HEWL crystal which was successfully laser-processed was seeded in a supersaturated solution and then it grew larger than its original size (Fig. 10).[46] Polarized light microscopy and X-ray diffraction analysis showed that the resulting crystal grown by seeding was a single crystal of suitable quality for X-ray crystallography. Thus, this deep-UV laser ablation seeding technique is useful for the production of seed crystals of adequate size and shape in macroseeding as well as for the elimination of a damaged section in a growing crystal.

3.2. Microseeding by femtosecond laser ablation

Microseeding, which conventionally utilizes small crystals (~μm) produced by crushing original crystals, has been demonstrated by femtosecond laser ablation. The technique was originally developed for the microseeding of urea crystals in supersaturated solutions.[47] A small region (~1 μm^2) of a urea crystal was ablated by irradiation with a near-infrared femtosecond laser pulse. Then a single, newly formed urea crystal appeared near the laser focal spot on the original

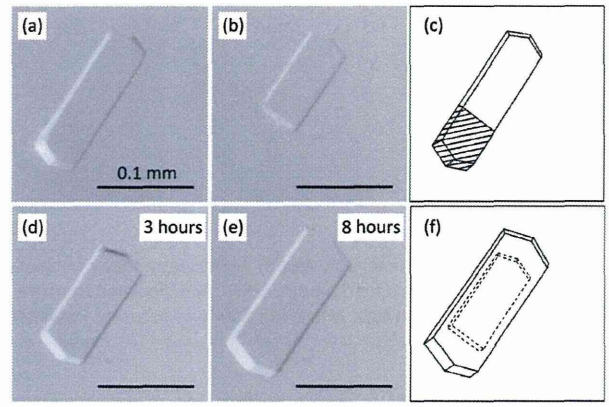

Fig. 10 Macroseeding of protein crystals by deep-UV laser ablation. (a) An as-grown HEWL crystal before laser ablation. (b) A seed crystal produced by laser ablation of the crystal in (a). (c) Outline of the crystal with ablated (hatched) and non-ablated regions shown. (d) and (e) Growth of the seed crystal at 3 and 8 h after laser ablation, respectively. (f) Outlines of the crystals immediately after laser ablation (dotted line) and after 8 h (solid line). Reprinted with permission from the Japan Society of Applied Physics, ref. 46, 2005.

(mother) crystal and grew independently. A single crystal fragment which was of the same size as the laser focal spot was ejected, and this fragment then acted as the seed crystal.

Given the physical characteristics of femtosecond laser ablation listed below, the advantages of the microseeding technique for protein can be explained as follows. (1) Focused irradiation with a near-infrared femtosecond laser induces ablation *via* multiphoton absorption, which should enable the spatially precise isolation of seed crystals from an arbitrary area of the mother crystals while present in a supersaturated solution. Conversely, irradiation with a deep-UV laser cannot reach a protein crystal in a supersaturated solution owing to the high absorption of UV light by the protein solute.[12] The dimension of spatial accuracy of femtosecond laser ablation *via* multiphoton absorption is similar to that of the laser focal spot, ~1 μm, which is small enough to precisely target the mother crystals. (2) Femtosecond laser ablation produces less heat than does ablation by other lasers with longer pulse width. The mechanism of femtosecond laser ablation just above the ablation threshold fluence is ascribed to a photomechanical process;[7] mechanical stress is confined to the excited region of the mother crystals and disrupts the surface resulting in collective ejection of crystal fragments. Hence, photomechanical ablation reduces potential thermal damage to seed crystals. That is, it is a "soft" method for microseeding of protein crystals.

In 2012, the microseeding technique was applied to proteins. Fig. 11a shows snapshots of HEWL crystals produced by femtosecond laser ablation. A tetragonal crystal (daughter crystal) was obtained by ablating a tetragonal HEWL mother crystal with a single 0.2 μJ femtosecond laser pulse.[11] Daughter crystals were not obtained with laser irradiation below the ablation threshold (0.2 μJ), which was confirmed by atomic force microscope (AFM) imaging of the HEWL crystals. XRD proved that the daughter crystal was a single crystal with almost

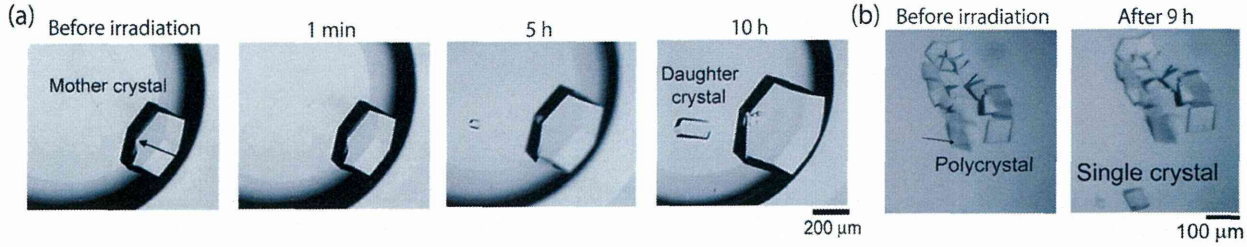

Fig. 11 Microseeding of protein crystals by femtosecond laser ablation. (a) Growth of HEWL microcrystals produced with a single femtosecond laser pulse. (b) Single crystal of the membrane protein, AcrB, isolated from the mother polycrystal by a single femtosecond laser pulse. The arrows point to the positions on the mother crystals where the laser was focused. Reprinted with permission from American Chemical Society, ref. 11, 2012.

the same crystallographic parameters (*e.g.*, the space group and unit-cell parameters) as those of the mother crystals. Notably, the daughter crystal diffracted to nearly the same resolution (1.47 Å) as the mother crystal did (1.46 Å), even though the daughter crystal was less than half the size of the mother crystal, suggesting that the quality of the daughter crystal was similar to that of the mother crystals. Such microseeding by femtosecond laser ablation was also demonstrated with polycrystals of a membrane protein, AcrB (Fig. 11b).[11] When the polycrystal was irradiated with a 0.3 μJ laser pulse (just above the ablation threshold (~0.2 μJ)), AcrB trigonal single crystals were obtained. AcrB crystals contain ~90% water, which made the production of seed crystals more difficult than for the HEWL system. Nevertheless, given the ability to produce AcrB daughter crystals, femtosecond laser ablation has the potential to produce microseeds of other recalcitrant proteins.

To assess the impact of femtosecond multiphoton, photomechanical ablation on the growth of single crystal microseeds, the surface of a HEWL mother crystal was observed using AFM.[11] Fig. 12a shows a representative image of a mother crystal surface etched using an ablation threshold (0.2 μJ per pulse). The etching is ~1 μm in diameter, which is much smaller than the laser spot size estimated by the diffraction limit (3.8 μm). Because HEWL crystals do not absorb 800 nm light, the region of the crystals impinged at the center of the laser spot is instead excited by multiphoton absorption, which decreases the diameter of the etching in comparison with etching formed by linear absorption. The crystal surface etched with a higher energy laser pulse (0.4 μJ per pulse) resulted in surface cracking (Fig. 12b). Notably, swelling was not observed surrounding the etched area. Such sharp etching and surface cracking strongly indicate that the crystal surface is mechanically disrupted *via* a photomechanical process, which should reduce critical thermal damage to HEWL molecules.

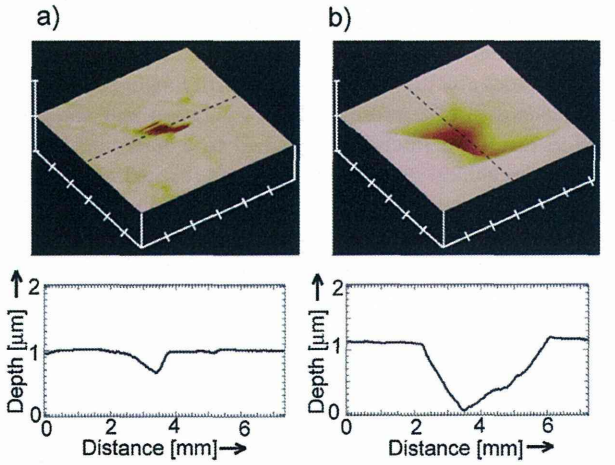

Fig. 12 (top) AFM images of HEWL crystal surfaces that were irradiated with a femtosecond laser pulse. (bottom) Depth profiles along the dotted line in the AFM images. Reprinted with permission from American Chemical Society, ref. 11, 2012.

Photomechanical ablation of protein crystals should result in ejection of bulky crystal fragments. If the surrounding solution is supersaturated and the ejected fragments are not significantly damaged, they can act as seed crystals. The molecular mechanism of the ejection of such bulky crystal fragments by photomechanical ablation has been intensively studied both experimentally and theoretically. Hosokawa *et al.* studied the ablation process on the basis of photoexcitation relaxation dynamics for a copper-phthalocyanine (CuPc) film,[48] where the molecules associate with each other *via* weak cohesion due to Van der Waals force as in the protein crystal case. Here, ultrafast temperature elevation, dT/dt ~100 °C/10 ps > 10^{13} °C s^{-1}, due to the rapid nonradiative relaxation (~20 ps) of highly excited electronic states formed by femtosecond laser excitation was observed. This implies that intramolecular and lattice vibrations are enhanced tremendously in a time scale of 10 ps, while the molecules are unable to change their positions from the equilibrium. As a result, mechanical stress accumulated in the film. If the laser energy is near the threshold of laser ablation, but still below plasma generation, the transient pressure mainly plays a role in causing morphological changes photomechanically, such as sharp surface etching and bulky fragment ejection with little thermal damage.[49] On the other hand, nanosecond laser ablation of the CuPc thin film is considered to involve relatively slow heating due to cyclic excitation,[50] which results in a gradual etching pattern and the ejection of molecularly dispersed ablated fragments. Using a molecular-level simulation technique, Zhigilei *et al.* also reported that photomechanical laser ablation of organic solids and liquids leads to disintegration and ejection of large relatively cold chunks of material.[41]

On the basis of the results, one can expect that femtosecond laser ablation *via* photomechanical processes results in the ejection of bulky crystal fragments with little damage, which can act as high-quality microseeds in supersaturated solutions. In addition, focused femtosecond laser irradiation enables the isolation of single protein microcrystals with high spatial accuracy in supersaturated solutions *via* multiphoton processes. Thus, the microseeding by femtosecond laser ablation will contribute to the production of high-quality protein single crystals from polycrystals or cracked crystals that are not suitable for XRD studies.

4. Conclusions and outlook

The utility and the underlying physico-chemical mechanism of laser ablation for protein crystal nucleation and seeding were reviewed. These successful results clearly show the potential of laser ablation techniques for the production of high-quality single crystals suitable for XRD studies. The key to the successful application of laser ablation to protein crystallization involves the use of lasers with ultrashort pulse widths or wavelengths (*e.g.* a femtosecond or a deep-UV laser), which allows for the spatially precise, low-damage processing of protein solutions and crystals *via* specific ablation processes (*e.g.*, photomechanical or photochemical). Although femtosecond and deep-UV lasers are a bit costly (>$100 000), the integration of laser ablation techniques in structural determination processes such as purification, crystallization, and XRD will accelerate advancement in the structural biology field. Laser ablation techniques are fully non-contact means that do not require significant changes in the conventional protein crystallization setup, and thus their application in automated and high-throughput screening/processing systems for protein crystallization is feasible in practice. In fact, Mori *et al.* have developed a system wherein conventional crystallization plates containing sub micro-liter solutions with sitting-drop or hanging-drop positions can be mounted on a motorized stage and irradiated with femtosecond laser pulses automatically.[10] High-quality protein single crystals produced using such an automated system will enhance the database of knowledge in structural biology and subsequent structure-based drug design.

Acknowledgements

This review is based upon works supported in part by grants from the Japan Society of the Promotion of Science (KAKENHI Nos. 24656006, 24680050, and 24106505 to HYY and 23360011 to YM and HYY).

References

1 I. D. Hoffman, *Methods Mol. Biol.*, 2012, **841**, 67–91.
2 I. Russo Krauss, A. Merlino, A. Vergara and F. Sica, *Int. J. Mol. Sci.*, 2013, **14**, 11643–11691.
3 U. Heinemann, K. Bussow, U. Mueller and P. Umbach, *Acc. Chem. Res.*, 2003, **36**, 157–163.
4 A. McPherson, *Crystallization of Biological Molecules*, Cold Spring Harbor Laboratory Press, New York, 1999.
5 B. A. Garetz, J. E. Aber, N. L. Goddard, R. G. Young and A. S. Myerson, *Phys. Rev. Lett.*, 1996, 77, 3475–3476.
6 A. Vogel, J. Noack, G. Huttman and G. Paltauf, *Appl. Phys. B: Lasers Opt.*, 2005, **81**, 1015–1047.
7 G. Paltauf and P. E. Dyer, *Chem. Rev.*, 2003, **103**, 487–518.
8 H. Adachi, Y. Hosokawa, K. Takano, F. Tsunesada, H. Masuhara, M. Yoshimura, Y. Mori and T. Sasaki, *J. Jpn. Assoc. Cryst. Growth*, 2002, **29**, 445–449 (in Japanese).
9 H. Adachi, K. Takano, Y. Hosokawa, T. Inoue, Y. Mori, H. Matsumura, M. Yoshimura, Y. Tsunaka, M. Morikawa, S. Kanaya, H. Masuhara, Y. Kai and T. Sasaki, *Jpn. J. Appl. Phys., Part 2*, 2003, **42**, L798–L800.
10 Y. Mori, K. Takano, H. Adachi, T. Inoue, S. Murakami, H. Matsumura, M. Kashii, H. Y. Yoshikawa, S. Maki, T. Kitatani, S. Okada and T. Sasaki, *Proc. SPIE*, 2007, **6460**, 646008.
11 H. Y. Yoshikawa, Y. Hosokawa, R. Murai, G. Sazaki, T. Kitatani, H. Adachi, T. Inoue, H. Matsumura, K. Takano, S. Murakami, S. Nakabayashi, Y. Mori and H. Masuhara, *Cryst. Growth. Des.*, 2012, **12**, 4334–4339.
12 H. Kitano, H. Adachi, A. Murakami, H. Matsumura, K. Takano, T. Inoue, Y. Mori, S. Owa and T. Sasaki, *Jpn. J. Appl. Phys., Part 2*, 2004, **43**, L73–L75.
13 I. Yoshizaki, T. Sato, N. Igarashi, M. Natsuisaka, N. Tanaka, H. Komatsu and S. Yoda, *Acta Crystallogr., Sect. D: Biol. Crystallogr.*, 2001, **57**, 1621–1629.
14 H. Y. Yoshikawa, R. Murai, S. Sugiyama, G. Sazaki, T. Kitatani, Y. Takahashi, H. Adachi, H. Matsumura, S. Murakami, T. Inoue, K. Takano and Y. Mori, *J. Cryst. Growth*, 2009, **311**, 956–959.
15 H. Adachi, S. Murakami, A. Niino, H. Matsumura, K. Takano, T. Inoue, Y. Mori, A. Yamaguchi and T. Sasaki, *Jpn. J. Appl. Phys., Part 2*, 2004, **43**, L1376–L1378.
16 S. Murakami, R. Nakashima, E. Yamashita and A. Yamaguchi, *Nature*, 2002, **419**, 587–593.
17 T. Tsukazaki, H. Mori, S. Fukai, T. Numata, A. Perederina, H. Adachi, H. Matsumura, K. Takano, S. Murakami, T. Inoue, Y. Mori, T. Sasaki, D. G. Vassylyev, O. Nureki and K. Ito, *Acta Crystallogr., Sect. F: Struct. Biol. Cryst. Commun.*, 2006, **62**, 376–380.
18 T. Numata, Y. Ikeuchi, S. Fukai, H. Adachi, H. Matsumura, K. Takano, S. Murakami, T. Inoue, Y. Mori, T. Sasaki, T. Suzuki and O. Nureki, *Acta Crystallogr., Sect. F: Struct. Biol. Cryst. Commun.*, 2006, **62**, 368–371.
19 Y. Sogabe, T. Kitatani, A. Yamaguchi, T. Kinoshita, H. Adachi, K. Takano, T. Inoue, Y. Mori, H. Matsumura, T. Sakamoto and T. Tada, *Acta Crystallogr., Sect. D: Biol. Crystallogr.*, 2011, **67**, 415–422.
20 Y. Hosokawa, H. Adachi, M. Yoshimura, Y. Mori, T. Sasaki and H. Masuhara, *Cryst. Growth. Des.*, 2005, **5**, 861–863.
21 H. Y. Yoshikawa, Y. Hosokawa and H. Masuhara, *Jpn. J. Appl. Phys., Part 2*, 2006, **45**, L23–L26.
22 K. Nakamura, Y. Hosokawa and H. Masuhara, *Cryst. Growth. Des.*, 2007, 7, 885–889.

23 T. H. Liu, T. Uwada, T. Sugiyama, A. Usman, Y. Hosokawa, H. Masuhara, T. W. Chiang and C. J. Chen, *J. Cryst. Growth*, 2013, **366**, 101–106.
24 S. Nakayama, H. Y. Yoshikawa, R. Murai, M. Kurata, M. Maruyama, S. Sugiyama, Y. Aoki, Y. Takahashi, M. Yoshimura, S. Nakabayashi, H. Adachi, H. Matsumura, T. Inoue, K. Takano, S. Murakami and Y. Mori, *Cryst. Growth. Des.*, 2013, **13**, 1491–1496.
25 F. Tsunesada, T. Iwai, T. Watanabe, H. Adachi, M. Yoshimura, Y. Mori and T. Sasaki, *J. Cryst. Growth*, 2002, **237–239**(Part 3), 2104–2106.
26 Y. Tsuboi, T. Shoji and N. Kitamura, *Jpn. J. Appl. Phys., Part 2*, 2007, **46**, L1234–L1236.
27 T. Sugiyama, T. Adachi and H. Masuhara, *Chem. Lett.*, 2007, 1480–1481.
28 H. Y. Yoshikawa, R. Murai, S. Maki, T. Kitatani, S. Sugiyama, G. Sazaki, H. Adachi, T. Inoue, H. Matsumura, K. Takano, S. Murakami, T. Sasaki and Y. Mori, *Appl. Phys. A: Mater. Sci. Process.*, 2008, **93**, 911–915.
29 A. Vogel and V. Venugopalan, *Chem. Rev.*, 2003, **103**, 577–644.
30 R. Murai, H. Y. Yoshikawa, Y. Takahashi, M. Maruyama, S. Sugiyama, G. Sazaki, H. Adachi, K. Takano, H. Matsumura, S. Murakami, T. Inoue and Y. Mori, *Appl. Phys. Lett.*, 2010, **96**, 043702.
31 N. Iefuji, R. Murai, M. Maruyama, Y. Takahashi, S. Sugiyama, H. Adachi, H. Matsumura, S. Murakami, T. Inoue, Y. Mori, Y. Koga, K. Takano and S. Kanaya, *J. Cryst. Growth*, 2011, **318**, 741–744.
32 R. G. Davey and J. Garside, *From Molecules to Crystallizers*, Oxford University Press, Oxford, 2000.
33 K. Nakamura, Y. Sora, H. Y. Yoshikawa, Y. Hosokawa, R. Murai, H. Adachi, Y. Mori, T. Sasaki and H. Masuhara, *Appl. Surf. Sci.*, 2007, **253**, 6425–6429.
34 J. Noack, D. X. Hammer, G. D. Noojin, B. A. Rockwell and A. Vogel, *J. Appl. Phys.*, 1998, **83**, 7488–7495.
35 M. Frenz, F. Konz, H. Pratisto, H. P. Weber, A. S. Silenok and V. I. Konov, *J. Appl. Phys.*, 1998, **84**, 5905–5912.
36 R. Hickling, *Phys. Rev. Lett.*, 1994, **73**, 2853–2856.
37 T. Okutsu, K. Furuta, M. Terao, H. Hiratsuka, A. Yamano, N. Ferte and S. Veesler, *Cryst. Growth Des.*, 2005, **5**, 1393–1398.
38 T. Okutsu, *J. Photochem. Photobiol., C*, 2007, **8**, 143–155.
39 R. Murai, H. Y. Yoshikawa, H. Hasenaka, Y. Takahashi, M. Maruyama, S. Sugiyama, H. Adachi, K. Takano, H. Matsumura, S. Murakami, T. Inoue and Y. Mori, *Chem. Phys. Lett.*, 2011, **510**, 139–142.
40 K. Kakinouchi, H. Adachi, H. Matsumura, T. Inoue, S. Murakami, Y. Mori, Y. Koga, K. Takano and S. Kanaya, *J. Cryst. Growth*, 2006, **292**, 437–440.
41 L. V. Zhigilei and B. J. Garrison, *J. Appl. Phys.*, 2000, **88**, 1281–1298.
42 B. C. Knott, J. L. Larue, A. M. Wodtke, M. F. Doherty and B. Peters, *J. Chem. Phys.*, 2011, **134**, 171102.
43 A. R. Goldfarb, L. J. Saidel and E. Mosovich, *J. Biol. Chem.*, 1951, **193**, 397–404.
44 H. Kitano, S. Murakami, H. Adachi, H. Matsumura, K. Takano, T. Inoue, Y. Mori, M. Doi and T. Sasaki, *J. Biosci. Bioeng.*, 2005, **100**, 50–53.
45 A. Murakami, H. Kitano, H. Adachi, H. Matsumura, K. Takano, T. Inoue, Y. Mori, M. Doi and T. Sasaki, *Jpn. J. Appl. Phys., Part 2*, 2004, **43**, L873–L876.
46 K. Takeuchi, H. Kitano, H. Adachi, Y. Mori, T. Sasaki, H. Matsumura, T. Inoue, S. Murakami, M. Doi, Y. Koga, K. Takano and S. Kanaya, *Jpn. J. Appl. Phys., Part 1*, 2005, **44**, 3177–3179.
47 H. Y. Yoshikawa, Y. Hosokawa and H. Masuhara, *Cryst. Growth Des.*, 2006, **6**, 302–305.
48 Y. Hosokawa, M. Yashiro, T. Asahi and H. Masuhara, *J. Photochem. Photobiol., A*, 2001, **142**, 197–207.
49 T. Asahi, H. Y. Yoshikawa, M. Yashiro and H. Masuhara, *Appl. Surf. Sci.*, 2002, **197**, 777–781.
50 H. Fujiwara, H. Ishii, T. Ishiwata, T. Hayashi, H. Fukumura and H. Masuhara, *Bull. Chem. Soc. Jpn.*, 2003, **76**, 1075–1085.

Journal of Bioscience and Bioengineering
VOL. xx No. xx, 1–6, 2014

ELSEVIER

www.elsevier.com/locate/jbiosc

Crystal structure of streptavidin mutant with low immunogenicity

Tatsuya Kawato,[1,‡] Eiichi Mizohata,[1,‡] Tomohiro Meshizuka,[1] Hirofumi Doi,[2] Takeshi Kawamura,[2] Hiroyoshi Matsumura,[1] Kyohei Yumura,[3,4] Kouhei Tsumoto,[3,4] Tatsuhiko Kodama,[2] Tsuyoshi Inoue,[1] and Akira Sugiyama[5,*]

Division of Applied Chemistry, Graduate School of Engineering, Osaka University, 2-1 Yamadaoka, Suita, Osaka 565-0871, Japan,[1] Research Center for Advanced Science and Technology, The University of Tokyo, Tokyo 153-8904, Japan,[2] Institute of Medical Science, The University of Tokyo, Minato-ku, Tokyo 108-8639, Japan,[3] Department of Medical Genome Sciences, Graduate School of Frontier Sciences, The University of Tokyo, Kashiwa 277-8562, Japan,[4] and Radioisotope Center, The University of Tokyo, 2-11-16 Yayoi, Bunkyo-ku, Tokyo 113-0032, Japan[5]

Received 17 September 2014; accepted 26 October 2014
Available online xxx

We previously created a low-immunogenic core streptavidin mutant No. 314 (LISA-314) by replacing six amino-acid residues for use as a delivery tool for an antibody multistep pre-targeting process (Yumura et al., Protein science, 22, 213–221, 2013). Here, we performed high-resolution X-ray structural analyses of LISA-314 and wild-type streptavidin to investigate the effect of substitutions on the protein function and the three-dimensional structure. LISA-314 forms a tetramer in the same manner as wild-type streptavidin. The binding mode of D-biotin in LISA-314 is also completely identical to that in wild-type streptavidin, and conformational changes were observed mostly at the side chains of substituted sites. Any large conformational changes corresponding to the reduction of *B* factors around the substituted sites were not observed. These results demonstrated the LISA-314 acquired low immunogenicity without losing structural properties of original wild-type streptavidin.

[**Key words:** Streptavidin; Low immunogenicity; Pre-targeting; Protein engineering; Crystal structure; X-ray structural analysis; *B* factor]

Cancer is the leading cause of death in economically developed countries and the second in developing countries. Worldwide, cancer accounts for 7.6 million deaths, and this is predicted to increase, with an estimated 13.1 million cancer-related deaths in 2030 (1). Development of innovative cancer therapies is therefore of utmost importance.

Targeted therapies such as antibody-drug conjugates, which treat cancer by targeting cancer-specific molecules, have been attracting much attention recently as they result in fewer side effects compared with standard chemotherapy (2,3). Pre-targeting drug delivery systems are expected to be especially beneficial by increasing both bio-imaging sensitivity and therapeutic effect over conventional systems, in which fluorescent markers for imaging or radioisotopes for treatment are directly attached to antibodies (4–6). In the pre-targeting method, treatment is first performed with antibody vehicle, followed by administration of fluorescent marker or radioisotope, displaying more favorable tumor-targeting properties. Several preclinical studies have validated the advantages of this approach using the streptavidin-biotin system proposed by Goodwin (4–12).

The interaction between streptavidin (SA) and D-biotin (BTN) is known to have the highest non-covalent affinity (K_d = 10^{-14}–10^{-15} M) in nature (13,14), and this interaction has been used in many biotechnological applications (15–18). Anti-CD20 antibodies with streptavidin have been shown to augment the efficacy of radioimmunotherapy and decrease toxicity compared with a directly-labeled antibody (19). In the process of pre-targeting, cancer cells can be captured by the SA-fused antibody as the first drug. After the excretion of excess of the first drug, a biotinylated imaging marker or radioisotope as the second drug can be specifically delivered to the SA-fused antibody on the cancer cells.

However, SA from *Streptomyces avidinii* exhibits high immunogenicity in humans, and the direct use of wild-type SA (SA-WT) is not suitable for clinical use (4,20–22). A reduction of immunogenicity by site-directed mutagenesis is necessary for medical applications of SA, without impairing its function and stability. Subramanian and Adiga (23) studied immunologic properties of SA and performed a detailed comparison of the epitopes of SA with rabbit antisera. Six linear epitopes regions were proposed using epitope mapping, (residues 17–23, 33–43, 84–87, 96–103, 114–121, and 128–131). Meyer et al. (21) also reported a mutant SA with lowered reactivity for an anti-SA antibody by substituting charged or aromatic amino-acid residues that make-up putative conformational epitopes on the protein surface required for interaction with B cells. The substitutions, however, also increased the dissociation rate from biotin, suggesting that the BTN-binding function has been reduced. The mechanism of acquiring low immunogenicity is obscure, because no structural studies have been performed for the mutants with decreased immunogenicity.

* Corresponding author. Tel.: +81 3 5841 2886; fax: +81 3 5452 5232.
E-mail address: sugiyama@lsbm.org (A. Sugiyama).
‡ The first two authors contributed equally to this work.

1389-1723/$ – see front matter
http://dx.doi.org/10.1016/j.jbiosc.2014.10.025

Recently, we have succeeded in creating a low immunogenic SA mutant No. 314 (LISA-314), which has greatly decreased immunoreactivity against monkey antiserum without impairing biophysical properties including biotin binding and thermal stability (24,25). LISA-314 was designed for reducing reactivity against anti-SA-WT serum and the number of *in silico* T-cell epitopes, by introducing six amino-acid substitutions (Y22S/Y83S/R84K/E101D/R103K/E116N) at solvent-exposed charged and aromatic residues that were proposed to be involved in its immune recognition. Unlike previous strategies mainly using alanine or glycine, we considered the substitutions so that the electrostatic charge and functional moieties of the WT residues were preserved.

In this study, we performed structural analysis by X-ray crystallography, to evaluate the effect of substitutions inside LISA-314 on the protein function and the three-dimensional structure. The results demonstrate that LISA-314 acquired lowered immunogenicity while maintaining an intact tetrameric assembly, main chain frameworks, and BTN-binding mode at the same level as SA-WT. We demonstrated that LISA-314 has identical structural property to SA-WT and potential for clinical applications in pre-targeting drug-delivery systems.

MATERIALS AND METHODS

Expression and purification The core SA-WT and LISA-314 were cloned into cleavable eXact tag fusion pPAL7 vector (Bio-Rad Laboratories). For the expression, SA-WT and LISA-314 plasmids were transformed into the *Escherichia coli* BL21Star(DE3) strain, which was cultivated in Luria-Broth medium supplemented with 100 μg/mL ampicillin at 37°C. When the optical density (λ = 600 nm) reached a value of 0.5, 0.4 mM isopropyl-β-D-thiogalactopyranoside (IPTG) was added for induction. Cultivation was continued for approximately 24 h at 16°C. Cells were harvested by centrifugation at 4°C at 8000 ×*g* for 20 min and resuspended in extraction buffer (10 mM phosphate, 100 mM NaCl, Complete EDTA-free protease inhibitor cocktail tablets (Roche) and Benzonase (Novagen) at pH 7.2). The sample was lysed by passing through a French press twice at 12,000 lb/in^2. The lysate was centrifuged at 10,000 ×*g* for 30 min to remove the insoluble fraction. The supernatant was loaded onto a HiTrap SP HP (GE Healthcare) and eluted with a linear gradient of 0.1–1.0 M NaCl in 10 mM phosphate buffer at pH 7.2. The eluted protein was dialyzed against binding buffer for the eXact column (Bio-Rad Laboratories) containing 10 mM phosphate and 300 mM sodium acetate at pH 6.8. The sample was then loaded onto an eXact column and the column was washed with the binding buffer. The column was further washed with the binding buffer supplemented with 100 mM NaF and incubated to allow cleavage of the eXact-tag at 25°C for 1 h. The cleaved protein was collected in the flow-through and dialyzed against 10 mM phosphate buffer at pH 6.0 for SA-WT and pH 6.8 for LISA-314. The sample was loaded onto a hydroxyapatite column and eluted with a phosphate gradient (Bio-Rad Laboratories). The eluted protein was buffer-exchanged into gel-filtration buffer (150 mM Tris–HCl and 150 mM NaCl at pH 7.5) using a Vivaspin 30-kDa cutoff (GE Healthcare). BTN was added to the sample at excess molar ratio for the SA-WT or LISA-314. Further purification was carried out by gel-filtration chromatography using a HiLoad 26/600 Superdex 75 column (GE Healthcare). The purified sample was then concentrated to approximately 9.0 mg/mL, estimated by the absorbance at 280 nm.

Crystallization Crystallization was performed by the sitting-drop vapor-diffusion methods at 20°C in Violamo 96-well plates (As One, Osaka, Japan). Sixty microliters of the reservoir solution was added to each well of the 96-well plates. Crystals of SA-WT were obtained by mixing 0.5 μL of protein solution (9.0 mg/mL SA-WT, 150 mM Tris–HCl and 150 mM NaCl at pH 7.5) and 0.5 μL of reservoir solution (0.2 M ammonium sulfate, 0.1 M sodium acetate trihydrate and 24% (w/v) PEG4000 at pH 5.2). On the other hand, crystals of LISA-314 were prepared by mixing 0.5 μL of protein solution (9.0 mg/mL LISA-314, 150 mM Tris–HCl and 150 mM NaCl at pH 7.5) and 0.5 μL of reservoir solution [0.2 M ammonium sulfate, 0.1 M sodium acetate trihydrate and 24% (w/v) PEG4000 at pH 5.2]. Crystals were cryoprotected by the reservoir solution containing 30% glycerol.

X-ray data collection and processing All datasets were collected on the beamline BL44XU at SPring-8 (Harima, Japan) under −173°C. Data were indexed and scaled with the programs *DENZO and SCALEPACK from the HKL2000 program suite* (HKL Research). The structures were solved by the molecular replacement with the program Phaser (26) from the CCP4i package (27) using a core streptavidin structure (PDB ID: 2F01) as the search model. The resultant structures were manually modified to fit into the experimental electron density maps, using the program *Coot* (28), then refined with the program Refmac (29) from the CCP4i package. The results of the structural analysis are summarized in Table 1. Figures were prepared with Pymol (http://www.pymol.org/). The final structure coordinates and structure-factor amplitudes were deposited into the Protein Data Bank with IDs 3WYP for SA-WT and 3WYQ for LISA-314.

TABLE 1. Data collection and refinement statistics.

	SA-WT	LISA-314
Data collection		
Space group	$P2_1$	$C2$
Unit-cell parameters (Å, °)	a = 50.35, b = 97.70, c = 52.57, β = 112.29	a = 63.22, b = 67.07, c = 56.36, β = 116.68
Wavelength	0.90000	0.82000
Resolution (Å)	50-1.30 (1.32-1.30)	50-1.00 (1.04-1.00)
R_{sym} (%)[a]	4.6 (34.5)	4.7 (29.6)
$I/\sigma(I)$	23.4 (2.9)	30.7 (3.6)
Completeness (%)	96.0 (93.3)	95.4 (91.6)
Redundancy	3.0 (2.7)	4.3 (3.2)
Refinement		
Resolution	1.30	1.00
No. of reflections	104885	101796
R_{work} (%)[b]/R_{free} (%)[c]	13.1/17.9	13.7/16.3
No. of atoms		
Protein	3697	1805
Ligand/ion	136	109
Water	480	254
B factors		
Protein	9.2	8.4
Ligand/ion	16.3	18.5
Water	29.3	28.1
R.m.s deviations		
Bond length (Å)	0.025	0.026
Bond angles (°)	2.23	2.43
Ramachandran plot		
Favored (%)	95.30	96.04
Allowed (%)	3.42	3.52
Outliers (%)	1.28	0.44

Values in parentheses are for the highest-resolution shell.

[a] R_{sym} is calculated as $\Sigma_{hkl}\Sigma_i|I_i(hkl) - \langle I(hkl)\rangle|/\Sigma_{hkl}\Sigma_i I(hkl)$, where $I_i(hkl)$ is the intensity of an individual measurement of the reflection with Miller indices *hkl* and $\langle I(hkl)\rangle$ is the average intensity from multiple observations.

[b] $R_{work} = \Sigma_{hkl}||F_{obs}| - |F_{calc}||/\Sigma_{hkl}|F_{obs}|$, where F_{obs} and F_{calc} are the observed and calculated structure-factor amplitudes, respectively.

[c] R_{free} is computed in the same manner as R_{work} but using only a small set (5%) of randomly chosen intensities that were not used in the refinement of the model.

RESULTS

Overview of the structure of LISA-314 Many structural analyses of SA have been reported previously (30–35). To perform a detailed structural comparison between LISA-314 and SA-WT, we determined their high-resolution crystal structures in complex with biotin (Table 1) by using the same protein expression, purification, and crystallization conditions. In the asymmetric unit, two protomers are contained in LISA-314 and four in SA-WT.

LISA-314 forms a tetramer in a similar manner to SA-WT (Fig. 1A). Each subunit consists of an eight-stranded β-barrel with a ligand binding site at one end of the barrel. The root mean squared deviation (RMSD) value for the Cα carbon atoms of the whole structure between LISA-314 and SA-WT is calculated to be 0.70 Å, but the RMSD value for each protomer is actually calculated to be lower (0.50–0.70 Å). Except for part of the C-terminal region, the main chains of the protomer in LISA-314 superimpose well with those in SA-WT, even at substituted sites (Fig. 1B, Table 2).

The BTN-binding mode of LISA-314 In 2/4 protomers of SA-WT, the sulfur atom of BTN is oxidized, so we compared the BTN-binding mode of LISA-314 with the other 2/4 chains of SA-WT containing non-sulfoxide BTN. The sulfoxide form of BTN is sometimes seen in the crystal structure of the SA-BTN complex, even though it was not added in purification or crystallization step (36,37). The BTN-binding mode of LISA-314 is the same as that of SA-WT, showing that the RMSD value for the BTN molecule between SA-WT and LISA-314 is only 0.05 Å. The BTN molecule

Please cite this article in press as: Kawato, T., et al., Crystal structure of streptavidin mutant with low immunogenicity, J. Biosci. Bioeng., (2014), http://dx.doi.org/10.1016/j.jbiosc.2014.10.025

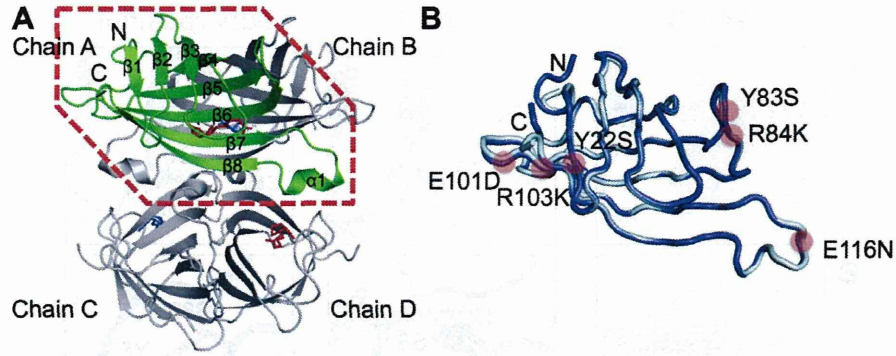

FIG. 1. Crystal structures of SA-WT and LISA-314. (A) The overall structure of SA-WT depicted in ribbon diagram. In the tetramer, one of the protomers is shown in green, and the other three protomers are shown in gray. In the four protomers, 2 BTN (shown in red) and 2 biotin-D-sulfoxide (shown in blue) molecules are bound in the active sites. (B) Main chain tracing for SA-WT (pale cyan) and LISA-314 (blue) after superposition on protomer. Substituted residues are shown by a red circle. (For interpretation of the references to colour in this figure legend, the reader is referred to the web version of this article.).

was stabilized by an extensive network of hydrogen bonds and van der Waals interactions as is seen in SA-WT (Fig. 2).

Conformational changes at substituted sites and *B* factors The structural change at every substitution site is summarized in Fig. 3, and the change of temperature (*B*) factors for all Cα carbon atoms is shown in Fig. 4. The *B* factor reflects the local mobility of protein backbones. We observed significant increases for *B* factors, which was not caused by packing effect, around the substitution sites of Y83S and R84K. The electron density maps for the side chain of Y83 of SA-WT and S83 of LISA-314 are well ordered, and main chains near the residues are well superimposed (Fig. 3B). However, the hydrogen bond between R84 and N49, which was found in SA-WT, was broken owing to the substitutions of R84K and Y83S in LISA-314 (Fig. 3C), and the *B* factors of the residues around these substituted residues were increased (Fig. 4). In all the substitutions, a slight decrease in *B* factor was only observed by the substitution of E101D. The electron density map for D101 of LISA-314 was improved after the introduction of shorter aspartate residue and the reduction of flexibility compared to E101 of SA-WT (Fig. 3D). Interestingly, the space group of the crystal of LISA-314 changed to *C*2 from the $P2_1$ of the SA-WT, even though both crystals were obtained using the same crystallization conditions. We try to rationalize this difference in the crystal packing below.

The conformational changes were mainly caused by the substitutions of Y22S and R103K (Fig. 3A and E), but the *B* factors were not affected (Fig. 4). One change is the flip of the C-terminal loop (residues 133–134) owing to the substitution of Y22S. The disappearance of the CH/π interaction between Y22 and K134 near the C-terminus is thought to be the reason for the flip as it is sometimes observed in the SA structures deposited in the Protein Data Bank. The second is the change in the hydrogen bond network resulting from the substitution of R103K. The hydrogen bond between R103 and T129, which was formed in 2/4 chains of SA-WT, was changed to that between K103 and T131 (a new hydrogen bond partner) as a result of the substitution. The last substitution site at E116N did not change the *B* factor, although the electron density for the side chain of N116 was clearly obtained (Fig. 3F).

Other than these substitution sites, we observed decreased *B* factors at residue numbers 32–35. The crystal packing was changed from *C*2 to $P2_1$ owing to the substitution of Y22S, and this region interacted with a neighboring molecule in the new crystal form, which may be the reason for the decrease in *B* factors.

TABLE 2. RMSD values (Å) for superposed streptavidin subunits.[a]

		SA-WT			
		A	B	C	D
LISA-314	A	0.54	0.59	0.62	0.50
	B	0.64	0.69	0.73	0.68

[a] Cα atoms were used for the structural superpositions.

DISCUSSION

The X-ray crystallography analyses of LISA-314 and SA-WT at high resolution revealed that LISA-314 forms a tetramer in the same manner as SA-WT, and the main chains are essentially identical to those of SA-WT except for a part of the C-terminus. The current study demonstrates that the binding mode of BTN in LISA-314 is completely identical to that of SA-WT, as all hydrogen bonds and van der Waals interactions are well conserved. This result strongly indicates that LISA-314 has the same BTN-binding function as that of SA-WT, although the binding constants measured by isothermal

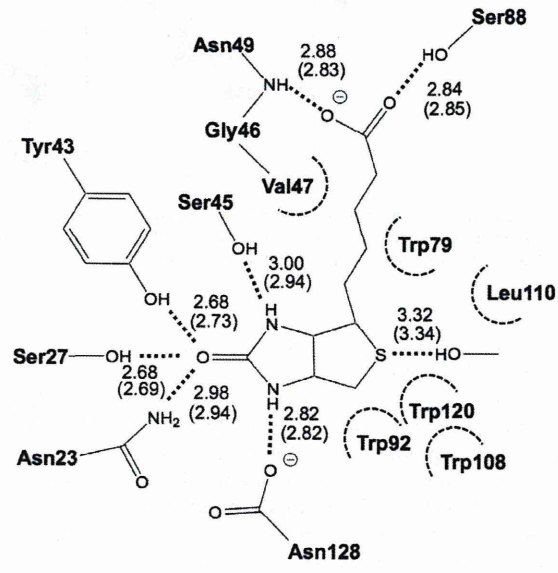

FIG. 2. Schematic representation of the interactions between BTN and LISA-314 or SA-WT. Dashed lines represent hydrogen bonds. The distances (Å) between residues of LISA-314 or SA-WT (parentheses) and BTN are shown.

Please cite this article in press as: Kawato, T., et al., Crystal structure of streptavidin mutant with low immunogenicity, J. Biosci. Bioeng., (2014), http://dx.doi.org/10.1016/j.jbiosc.2014.10.025